This is the Pre-Published Version.

The following publication J. Wen, Z. Sun, X. Yuan, S. Niu, Z. Lyu and K. -T. Chau, "Robust Model Predictive Control of Electrical Drives Considering Measurement Noises," in IEEE Transactions on Transportation Electrification, vol. 11, no. 6, pp. 13126-13138, Dec. 2025 is available at https://doi.org/10.1109/TTE.2025.3600636.

Robust Model Predictive Control of Electrical Drives Considering Measurement Noises

Junkai Wen, Zhenyao Sun, Xin Yuan, *Senior Member, IEEE*, Shuangxia Niu, *Senior Member, IEEE*, Zekai Lyu, *Member, IEEE*, and K.T. Chau, *Fellow, IEEE*

***Abstract*—In the realm of model predictive current control (MPC) for electrical drives, the multiple vector MPC offers significant advantages with respect to its high current tracking accuracy and reduced current ripples, making it a promising alternative to conventional single-vector MPC. To compensate for the system disturbances due to model mismatches, extended-state observers (ESOs) are often integrated. However, the observer bandwidth relating to the disturbance rejection capability is usually compromised, since high bandwidth will inevitably amplify high-frequency measurement noises. To address this coupling issue between high frequency noises in steady state current and the disturbance rejection capability in transient scenarios, a novel triple-vector MPC is proposed in this paper. Specifically, the MPC incorporating an active damping method is proposed to improve the robustness against parameter mismatch and disturbances. Moreover, a dedicated adaptive current predictor is proposed to estimate current with one step delay compensation, where an additional coefficient is designed to suppress measurement noises independently. To further enhance the flexibility of the current predictor, the adaptive mechanism based on the operation status is introduced to adjust the introduced coefficient. Comprehensive experiments have been conducted to demonstrate the superiority in both high robustness and noise suppression of the proposed controller.**

***Index Terms*—ESO, electrical drive, MPC, noise suppression, three level inverter, multiple vectors.**

I. Introduction

DUE to high power density, large torque capability, and high efficiency, PMSMs have been widely applied in the fields of the industry and transportation [1] [2]. The reliability of PMSM drive systems is significantly essential for the above-mentioned applications. Conventional control methods of PMSMs drives are field-oriented control (FOC) and direct torque control (DTC). Although FOC can achieve good steady-state performance and low current ripple, it has difficulty in adapting the complicated vehicle motor conditions and needs much work during the gain-tuning [3], [4]. Compared to FOC, DTC has quicker dynamic response with simple structure and does not need pulsewidth modulation (PWM) [5]. However, in general, poor steady-state performance, large current ripple and variable switching frequency in DTC schemes are difficult to be avoided [6].

Recently, model predictive control (MPC) has attracted increasing attention within the field of motor drives due to its superior capability in effectively handling uncertainties, nonlinearities, and constraints [7], [8]. Different from DTC, MPC can generate the optimal voltage vector by minimizing the error between the reference value and predictive value [9]. However, the conventional MPC only use one vector in each sampling period, there is a voltage error between the selected voltage vector and the reference voltage vector, which affects the steady-state control performance to a certain extent [10]. Hence, large current ripple and low noise robustness are two shortcomings that obstruct the development of conventional single-vector MPC. The steady-state performance of MPC can be improved by increasing the sampling frequency and extending the prediction horizon. However, this can lead to increased computational burden and higher hardware expenses. In this case, multiple-vector control methods were developed to enhance the steady-state performance of MPC, where multiple voltage vectors are applied during a single control period to reduce the current ripple [11]. A double vector MPC using dual active vector was proposed in [12]. The duration times of the two vectors are determined based on the tracking error minimization principle. Zhang et al. [13] proposed an improved double MPC to further enhance the steady state performance, where the second voltage vector is not fixed as a null vector but is instead selected within a boundary range. [14] proposed a double vector MPC using virtual voltage vectors to mitigates the common mode voltages, where the small voltage vectors with high common mode voltage is synthesized by adjacent voltage vectors. In order to further improve steady-state performance, triple-vector MPC (TVMPC) was proposed, where three voltage vectors are utilized within each control cycle [15]–[17]. Guo et al. proposed a novel visualization analysis method to evaluate the effectiveness of the triple-vector MPC method [18]. Besides, in [19], a symmetrical triple-vectpr MPC is also developed to further enhance the steady-state performance of PMSMs.

Since the performance of the MPC predictive scheme highly relied on parameter accuracy and only the feedback error regulation will not change the model's low dynamic stiffness and damping characteristics, one notable shortcoming of MPC is insufficient disturbance rejection. For example, the distur-

This work was supported in part by the Research Grant Council of the Hong Kong Government under Projects PolyU 152109/20E and in part by RGC Collaborative Research Fund under Grant C1052-21G. (Junkai Wen and Zhenyao Sun contributed equally to this work.) (Corresponding author: Shuangxia Niu)

Junkai Wen, Zhenyao Sun, Shuangxia Niu, Zekai Lyu, and K.T. Chau are with the Department of Electrical and Electronic Engineering, The Hong Kong Polytechnic University, Hong Kong 999077, China (e-mail: zhenyao.sun@polyu.edu.hk; 22116996r@connect.polyu.hk; eesxniu@polyu.edu.hk; zekai.lyu@polyu.edu.hk; k.t.chau@polyu.edu.hk)

Xin Yuan is with the School of Engineering, University of Aberdeen, AB24 3UF Aberdeen, U.K. (e-mail: xin.yuan@abdn.ac.uk).

© 2025 IEEE. Personal use of this material is permitted. Permission from IEEE must be obtained for all other uses, in any current or future media, including reprinting/republishing this material for advertising or promotional purposes, creating new collective works, for resale or redistribution to servers or lists, or reuse of any copyrighted component of this work in other works.

bances caused by resistance and rotor flux linkage mismatch can lead to the current offset, and load torque disturbance can affect the stability of the system [20]–[22]. The main control methods for enhancing disturbance rejection are extended state observers (ESO) [23], [24] and active damping [25], [26]. The former method is widely applied in MPC, while the latter method is more frequently utilized in the current loop of FOC. The active damping method was initially designed in the continuous domain to enhance the dynamic stiffness of the system [27], where the feedback of the active resistance to the voltage command was proposed to improve the stiffness of the controller, which has a similar effect as increasing the physical resistance of the plant [28]. Subsequently, the active damping technique is extended to the discrete domain [29]. The optimal value for the active damping method was derived in [30], with the goal of enhancing disturbance rejection capability while simultaneously minimizing the adverse effects of active damping on the current response. ESO considers internal uncertainties, external disturbances, and unmodeled dynamics as total disturbances and estimates these disturbance concurrently with the state variables. Although ESOs can be categorized into linear and nonlinear types, linear ESOs are more favored due to their ease of analysis and well-established theoretical foundation [31]. In order to enhance the time-varying disturbance rejection, resonant extended state observers and high-order extended state observers were developed, the former is more sensitive to frequency variations and requires more information [32], [33]. However, since both disturbances and predicted values need to be obtained within the ESO, a notable weakness of ESO is its limited ability to suppress noise, which limits the control performance of the ESO. If noise sensitivity is reduced, its disturbance rejection capability will consequently be weakened. Moreover, as the order increases, its noise suppression ability decreases. Therefore, enhancing noise suppression capability without sacrificing disturbance rejection is crucial for both MPC and ESO.

Approaches are developed to decouple the tradeoff between the disturbance rejection and noise suppression ability of ESO. An additional integral state variable was proposed in [34] to expand the plant in the ESO structure, which partially decoupled noise and disturbance ability and improved the current smoothing. However, the integral term introduces an additional phase delay to the ESO, which affects the dynamic performance of the system. [35] proposed an adaptive switching high-order ESO, which switches the observer gain according to the tracking error to achieve better steady state and dynamic performance, but the design is more complicated. The cascade ESO was proposed and analyzed in [31], [36], it has been demonstrated to possess superior noise suppression capabilities compared to the standard ESO. Subsequently, low-power and high-order cascaded ESO techniques were developed to address the issues of noise amplification and challenges in numerical implementation [37]. However, increasing the number of ESOs introduces additional delays, which can affect the system's tracking speed and complicate the tuning process. In summary, although the aforementioned techniques improve the noise suppression capabilities of ESO, they can negatively impact signal tracking and convergence performance. Moreover, the aforementioned methods are predominantly applied in speed control loops and are rarely utilized in current control loops.

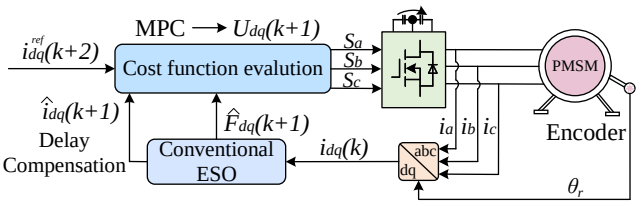

Fig. 1. The block diagram of the conventional MPC using ESO.

In this paper, a novel triple-vector MPC is proposed to decouple disturbance rejection and noise suppression capabilities while maintaining good dynamic response performance for the current loop. The main innovations of this paper can be listed as follows:

1) Different and superior to the method that the integral term introduces an additional phase delay to the ESO [34] and existing MPC using ESO structures, a novel discrete-time current predictor based on the superposition theorem is proposed to independently and directly predict the next instant current to decouple the noise suppression and disturbance rejection, where the noise suppression ability can be adjusted through the parameter of the current predictor. In the proposed structure, superior to ESO structures, there is no need to obtain the disturbance caused by the parameter mismatch, the application of the superposition theorem allows it to achieve good parameter robustness while maintaining a simple design process. Furthermore, an adaptive controller is applied to smooth the current and enable the controller to achieve both rapid tracking response and good steady-state performance.

2) Both cascaded ESOs and adaptive ESOs use observer structures to enhance the disturbance rejection ability of MPC, but they do not effectively solve the coupling problem. Additionally, these methods are mostly applied to the speed loop rather than the current loop. Motivated by this fact, aiming to independently improve the system's disturbance rejection, without using ESOs, this paper first introduces active damping combined with predictive current control into the framework of triple-vector MPC for the current loop.

This paper is organized as follows: Section II introduces the conventional MPC using ESO. Section III presents the design theory of the proposed frame work for MPC, the robust current predictor, and the proposed adaptive control method. Section IV provides experimental comparisons of the conventional MPC using ESO and the proposed controller. Finally, the work is concluded in Section V.

II. CONVENTIONAL MPC USING ESO

A. Design of Conventional MPC Using ESO

The voltage equation of the surface-mounted PMSM in synchronous reference frame by complex vector can be presented as follows [22]:

$$U_{dq} = R_s i_{dq} + L_s \dot{i}_{dq} + j\omega_e L_s i_{dq} + e_{dq} - F_{dq}, \qquad (1)$$

where $U_{dq} = U_d + jU_q$ denotes the stator voltage vector, $i_{dq} = i_d + ji_q$ denotes the current vector, and j is the imaginary unit. L_s represents the stator inductance, R_s represents the stator resistance. $e_{dq} = j\omega_e\psi_f$, where ω_e is the electrical angular speed and ψ_f is the permanent magnet flux. $F_{dq}$is the unknown disturbance in the system.

Based on (1), MPC methods can be employed to force future currents to track reference currents [38]. However, since actual SPMSM parameters may vary under different conditions, disturbance caused by parameter mismatches can deteriorate the performance of MPC. In order to solve this issue, ESO has been applied to MPC to estimate disturbances. The design of ESO can be presented as follows [3]:

$$\begin{aligned} e_{rr} =& \hat{i}_{dq} - i_{dq} \\ \dot{\hat{i}}_{dq} =& L_s^{-1}\left(U_{dq} - R_s\hat{i}_{dq} - j\omega_e L_s i_{dq} - e_{dq} + \hat{F}_{dq}\right) - \beta_1 e_{rr} \\ \dot{\hat{F}}_{dq} =& -\beta_2 e_{rr}, \end{aligned} \tag{2}$$

where $\hat{i}_{dq}$ and $\hat{F}_{dq}$ are the estimated current and estimated disturbance in ESO, respectively. β_1 and β_2 are the error feedback gains of ESO and can determine the comprehensive performance of the observer. According to [38], defining ω_0 as the bandwidth of ESO, β_1 and β_2 can be obtained as follows:

$$\begin{aligned} \beta_1 =& 2\omega_0 - \frac{R_s}{L_s} \\ \beta_2 =& \omega_0^2 L_s. \end{aligned} \tag{3}$$

Therefore, (2) can be modified as (4) by Euler-forward discretization and the $(k+1)$ th instant stator current $\hat{i}_{dq}(k+1)$ and estimated disturbance $\hat{F}_{dq}(k+1)$ can be easily obtained as follows [6]:

$$\begin{aligned} \hat{i}_{dq}(k+1) =& \left(1 - \frac{R_s T_s}{L_s}\right)\hat{i}_{dq}(k) + \frac{T_s}{L_s}U_{dq}(k) \\ & - j\omega_e T_s i_{dq}(k) + \frac{T_s}{L_s}\hat{F}_{dq}(k) - \frac{e_{dq}(k)\,T_s}{L_s} - \beta_1\frac{T_s}{L_s}e_{rr} \\ \hat{F}_{dq}(k+1) =& \hat{F}_{dq}(k) - \beta_2 e_{rr} T_s. \end{aligned} \tag{4}$$

Considering one-step delay in actual digital systems, the $(k+1)$ th instant reference voltage of MPC $U_{dq}^{ref}(k+1)$ can be obtained as follows:

$$\begin{aligned} U_{dq}^{ref}(k+1) =& \frac{L_s}{T_s}\left[i_{dq}^{ref}(k+2) - \hat{i}_{dq}(k+1)\right] + R_s\hat{i}_{dq}(k+1) \\ & + j\omega_e L_s\hat{i}_{dq}(k+1) + e_{dq}(k+1) - \hat{F}_{dq}(k+1). \end{aligned} \tag{5}$$

The block diagram of MPC using ESO is shown in Fig. 1.

B. Limitation of Conventional MPC Using ESO

It can be seen from (4) and Fig. 1 that whether it is the $(k+1)$ th instant stator current or the estimated disturbance, both need to be obtained within the ESO. Therefore, it is necessary to analyze the coupling issue between the disturbance rejection capability and noise suppression ability.

1) Disturbance rejection analysis: Frequency-domain disturbance rejection analysis for ESO gives the transfer function from the actual disturbance to the estimated error $G_{eF}(s)$, and from the actual disturbance to the estimated disturbance

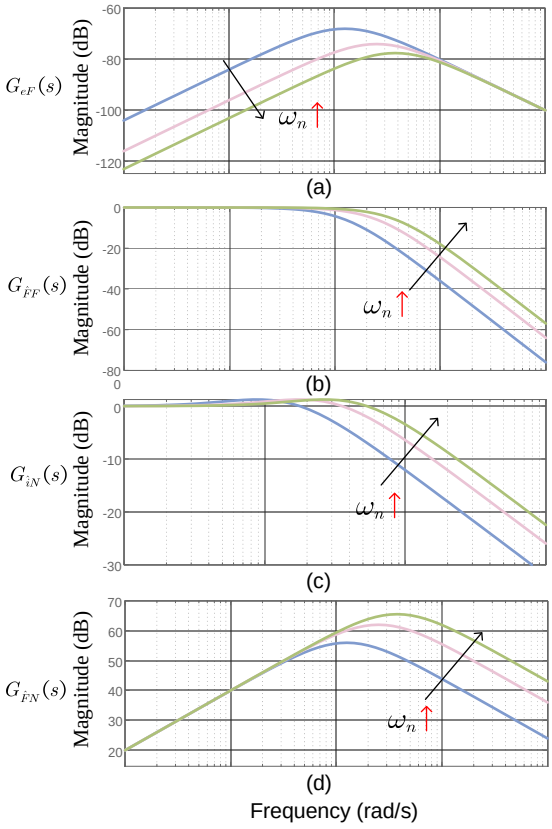

Fig. 2. Bode diagrams of the frequency-domain analysis for ESO.

$G_{\hat{F}F}(s)$. The detailed derivation is shown as follows: (6) can be obtained by substituting (2) into (1),

$$\dot{e}_{rr} = L_s^{-1}\hat{F}_{dq} - L_s^{-1}F_{dq} - L_s^{-1}R_s e_{rr} - \beta_1 e_{rr}, \tag{6}$$

Taking the Laplace transform of (2) and (6) [39],

$$e_{rr}s = L_s^{-1}\hat{F}_{dq} - L_s^{-1}F_{dq} - L_s^{-1}R_s e_{rr} - \beta_1 e_{rr}, \tag{7}$$

$$\hat{F}_{dq}s = -\beta_2 e_{rr}, \tag{8}$$

Substituting (8) into (7),

$$e_{rr}\left[s^2 + \left(\beta_1 + R_s L_s^{-1}\right)s + \beta_2 L_s^{-1}\right] = -L_s^{-1}F_{dq}s, \tag{9}$$

Therefore, the transfer function from the actual disturbance to the estimated error $G_{eF}(s)$ can be expressed as follows:

$$G_{eF}(s) = \frac{-sL_s^{-1}}{s^2 + \left(\beta_1 + R_s L_s^{-1}\right)s + \beta_2 L_s^{-1}}. \tag{10}$$

Similarly, substituting (7) into (8),

$$L_s^{-1}F_{dq}\beta_2 = \hat{F}_{dq}\left[s^2 + \left(\beta_1 + R_s L_s^{-1}\right)s + \beta_2 L_s^{-1}\right], \tag{11}$$

Therefore, the transfer function from the actual disturbance to the actual disturbance to the estimated disturbance $G_{\hat{F}F}(s)$ can be expressed as follows:

$$G_{\hat{F}F} = \frac{\hat{F}_{dq}(s)}{F_{dq}(s)} = \frac{L_s^{-1}\beta_2}{s^2 + \left(\beta_1 + R_s L_s^{-1} + \beta_2 L_s^{-1}\right)}. \tag{12}$$

Fig. 2 plots the frequency characteristics of $G_{eF}(s)$ and $G_{\hat{F}F}(s)$. It can be seen from Fig. 2 (a) that the low-frequency

disturbance rejection ability of ESO increases with the increase of bandwidth but the high-frequency noise suppression ability has not changed. Fig. 2 (b) shows the high bandwidth makes the ESO sensitive to high frequency disturbance.

2) Noise suppression analysis: Measurement noise is a critical non-ideal factor that must be considered in the motor drive control system, and it contains high-frequency components of different volumes. Theoretically, any unaccounted measurement noise will inherently affect the accuracy of the predictive controller. Since MPC aims to eliminate tracking errors in each cycle, studying its response to measurement noise is particularly important [40]. Frequency-domain noise suppression analysis for ESO gives the transfer function from the measurement noise to the estimated current $G_{\hat{i}N}(s)$ and the measurement noise to the estimated disturbance $G_{\hat{F}N}(s)$. Taking the Laplace transform of (2),

$$\hat{i}_{dq}s = L_s^{-1}\left(U_{dq} - j\omega_e L_s i_{dq} - e_{dq} + R_s\hat{i}_{dq} + \hat{F}_{dq}\right) - \beta_1 e_{rr} \tag{13}$$

$$\hat{F}_{dq}s = -\beta_2 e_{rr}, \tag{14}$$

Substituting (14) into (13),

$$\begin{aligned}\hat{i}_{dq}s^2 + \beta_2\hat{i}_{dq} + \beta_1\hat{i}_{dq}s = sL_s^{-1}\left(U_{dq} - j\omega_e L_s i_{dq} - e_{dq}\right)\\ + sL_s^{-1}\left(R_s\hat{i}_{dq} + \hat{F}_{dq}\right) + \left(\beta_2 + \beta_1 s\right)i_{dq},\end{aligned} \tag{15}$$

Considering the existence of the output side measuring noise $N_{dq}(s)$, (15) can be written as follows [41]:

$$\begin{aligned}\hat{i}_{dq} = \frac{sL_s^{-1}}{s^2 + \left(\beta_1 + R_sL_s^{-1}\right)s + \beta_2 L_s^{-1}}\left(U_{dq} - j\omega_e L_s i_{dq} - e_{dq}\right.\\ \left. + \hat{F}_{dq}\right) + \frac{\beta_1 s + \beta_2}{s^2 + \left(\beta_1 + R_sL_s^{-1}\right)s + \beta_2 L_s^{-1}}\left(i_{dq} + N_{dq}\right)\end{aligned} \tag{16}$$

Hence, the transfer function from the measurement noise to the estimated current $G_{\hat{i}N}(s)$ can be expressed as follows:

$$G_{\hat{i}N} = \frac{\hat{i}_{dq}(s)}{N_{dq}(s)} = \frac{\beta_1 s + \beta_2}{s^2 + \left(\beta_1 + R_sL_s^{-1}\right) + \beta_2 L_s^{-1}}. \tag{17}$$

Similarly, substituting (13) into (14),

$$\begin{aligned}\beta_2 i_{dq} =& \beta_2\frac{L_s^{-1}\left(U_{dq} - j\omega_e L_s - e_{dq} + R_s\hat{i}_{dq} + \hat{F}_{dq}\right) + \beta_1 i_{dq}}{s + \beta_1}\\ &+ \hat{F}_{dq}s\end{aligned} \tag{18}$$

Considering the existence of the output side measuring noise $N_{dq}(s)$, (18) can be written as follows:

$$\begin{aligned}\hat{F}_{dq} =& \frac{\beta_2 s}{s^2 + \left(\beta_1 + R_sL_s^{-1}\right) + \beta_2 L_s^{-1}}\left(i_{dq} + N_{dq}\right)\\ &- \frac{\beta_2 L_s^{-1}\left(U_{dq} - j\omega_e L_s i_{dq} - e_{dq}\right)}{s^2 + \left(\beta_1 + R_sL_s^{-1}\right)s + \beta_2 L_s^{-1}}\end{aligned} \tag{19}$$

Hence, the transfer function from the measurement noise to the estimated disturbance $G_{\hat{F}N}(s)$ can be expressed as follows:

$$G_{\hat{F}N} = \frac{\hat{F}_{dq}(s)}{N_{dq}(s)} = \frac{\beta_2 s}{s^2 + \left(\beta_1 + R_sL_s^{-1}\right)s + \beta_2 L_s^{-1}}. \tag{20}$$

The bode diagrams of $G_{\hat{i}N}(s)$ and $G_{\hat{F}N}(s)$ are shown in Fig. 2. As the bandwidth increases, the noise suppression ability of ESO decreases. Generally, to ensure satisfactory estimation accuracy and disturbance rejection capability, ESO is typically set to a high bandwidth. However, both uncertain current quantization noise and electromagnetic interference (EMI) noise contain high-frequency components. A high bandwidth makes the ESO more sensitive to noise, which can lead to adverse effects such as increased current ripple, oscillations in mechanical systems, and even system instability [42].

III. Proposed MPC

According to the analysis in Section II, the conventional ESO is hard to meet simultaneously in terms of requirements for disturbance rejection and measurement noise suppression in model predictive current control. For the purpose of solving the above-mentioned problem, a novel framework for MPC is proposed in this article to balance the disturbance rejection and noise suppression.

A. MPC With Active Damping Framework

Since all the signal including current controllers and inverters are implemented in the digital system, there is an inevitable execution time delay, which is commonly one sampling period. Hence, it is necessary to build the discrete-domain model considering execution delay instead of the continuous-domain model. Besides, in order to simplify an inverter model, inverter nonlinearity has been consistently compensated based on look-up-table(LUT) [38]. Based on (1) and (5), considering e_{dq} as a disturbance, the transfer function of the PMSM model $G_{p1}(z)$ with one-step delay compensation and the current controller $G_{c1}(z)$ based on internal model principle in the discrete-time domain can be presented as follows [43]:

$$\begin{aligned}G_{p1}(z) =& \frac{i_{dq}(z)}{U_{dq}(z)} = \frac{L_s^{-1}T_s}{z\left(z - 1 + j\omega_e T_s + R_sT_sL_s^{-1}\right)}\\ G_{c1}(z) =& \frac{a_1\left(z - 1 + j\omega_e T_s + R_sT_sL_s^{-1}\right)}{(z-1)L_s^{-1}T_s}.\end{aligned} \tag{21}$$

where a_1 is the bandwidth of the current controller and is set to 1 to achieve the deadbeat response in the MPC structure [26]. In this case, the disturbance rejection transfer function $G_{d1}(z)$, i.e., the current response produced by disturbance in the discrete-time domain can be derived as follows:

$$\begin{aligned}G_{d1}(z) =& \frac{i_{dq}(z)}{D_{dq}(z)} = \frac{G_{p1}(z)}{1 + zG_{c1}(z)G_{p1}(z)}\\ =& \frac{L_s^{-1}T_s(z-1)}{\left(z - 1 + j\omega_e T_s + R_sT_sL_s^{-1}\right)(z - 1 + a_1)z}.\end{aligned} \tag{22}$$

Fig. 4 plots the frequency characteristics of $G_{d1}(z)$. It can be seen that the disturbance rejection of the system is insufficient since only the feedback error regulation scheme in MPC can not change the PMSM plant's low stiffness and damping characteristics. To solve this issue, the active damping method with prediction scheme is introduced to MPC to enhance disturbance rejection ability. In this case, the transfer function

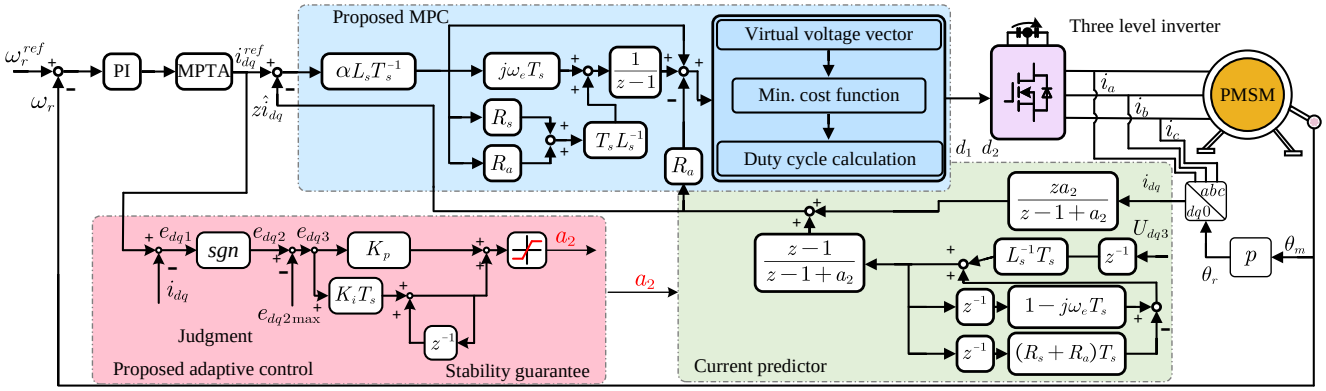

Fig. 3. Block diagrams of the proposed triple-vector MPC controller.

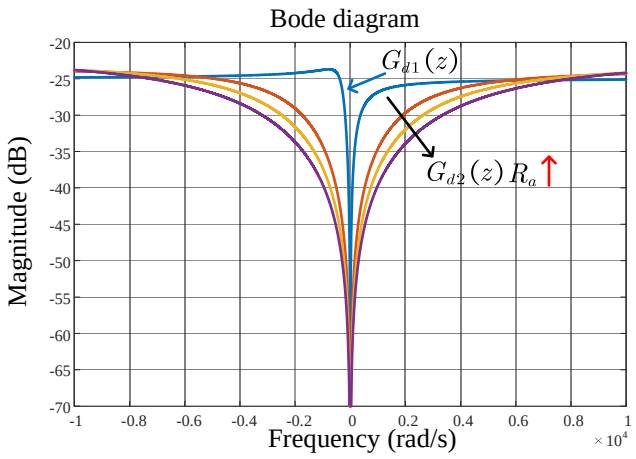

Fig. 4. Bode diagrams of the disturbance rejection evaluation.

of the PMSM model $G_{p2}(z)$ and the controller $G_{c2}(z)$ can be derived as follows:

$$G_{p2}(z)=\frac{i_{dq}(z)}{U_{dq}(z)}=\frac{L_s^{-1}T_s}{z\left(z-1+j\omega_eT_s+(R_s+R_a)T_sL_s^{-1}\right)}$$

$$G_{c2}(z)=\frac{a_1\left(z-1+j\omega_eT_s+(R_s+R_a)T_sL_s^{-1}\right)}{(z-1)L_s^{-1}T_s}. \tag{23}$$

(23) shows the active damping method with prediction scheme is composed of two parts: one-step lead operator z and the active resistance R_a. The one-step lead operator z can be implemented using a current predictor which will be designed later. In this case, the disturbance rejection transfer function of the proposed framework $G_{d2}(z)$, i.e., the current response produced by disturbance in the discrete-time domain can be derived as follows:

$$\begin{aligned}G_{d2}(z)=&\frac{i_{dq}(z)}{D_{dq}(z)}=\frac{G_{p2}(z)}{1+zG_{c2}(z)G_{p2}(z)}\\=&\frac{L_s^{-1}T_s(z-1)z^{-1}}{\left(z-1+j\omega_eT_s+(R_s+R_a)T_sL_s^{-1}\right)(z-1+a_1)}.\end{aligned} \tag{24}$$

Fig. 4 plots the frequency characteristics of $G_{d2}(z)$. After incorporating the proposed method, the system's disturbance rejection ability is significantly increased, and this ability is further improved as R_a increased. In order to maintain disturbance rejection while ensuring that the system operates in a high damped state, R_a is set to $0.246L_sT_s^{-1}$ in this article [43]. The block diagram of the proposed MPC is shown in Fig. 3. The digital implementation of the proposed framework is shown as follows:

$$\begin{cases}P_{dq1}(k)=a_1L_sT_s^{-1}\left(i_{dq}^{ref}(k+2)-\hat{i}_{dq}(k+1)\right)\\P_{dq2}(k)=P_{dq1}(k)\\\qquad -P_{dq1}(k-1)\left(1-j\omega_eT_s-(R_s+R_a)L_s^{-1}T_s\right)\\P_{dq3}(k)=P_{dq2}(k-1)+P_{dq3}(k-1)\\U_{dq}^{ref}(k+1)=P_{dq3}(k)+e_{dq}(k)-\hat{i}_{dq}(k+1)R_a.\end{cases} \tag{25}$$

B. Proposed Current Predictor

Aiming at predicting the next instant current independently while reducing the system's sensitivity to parameter mismatches and incorporating the active damping method, a robust current predictor is proposed in this section.

The proposed current predictor can be divided into a controller and a plant, where sampling current $i_{dq}(z)$, $z^{-1}U_{dq3}(z)$, the predicted current $z\hat{i}_{dq}(z)$ are considered as designed as input, disturbance, output, respectively. Compared to traditional current prediction schemes that do not consider disturbances caused by the parameter mismatch, the disturbance U_{dq4} can be obtained by the controller of the current predictor. Since the active damping method has been applied, the disturbance $z^{-1}U_{dq3}(z)$ at kth instant can be derived as follows:

$$z^{-1}U_{dq3}(z)=z^{-1}U_{dq}^{ref}(z)-j\omega_e\psi_f+\hat{i}_{dq}(z)R_a. \tag{26}$$

Hence, the plant of the current predictor $G_{pe}(z)$ can be designed based on (23) as follows:

$$\begin{aligned}G_{pe}(z)=&\frac{z\hat{i}_{dq}(z)}{z^{-1}U_{dq2}(z)}\\=&\frac{L_s^{-1}T_s}{1-z^{-1}+j\omega_eTz^{-1}+z^{-1}(R_s+R_a)L_s^{-1}T_s}.\end{aligned} \tag{27}$$

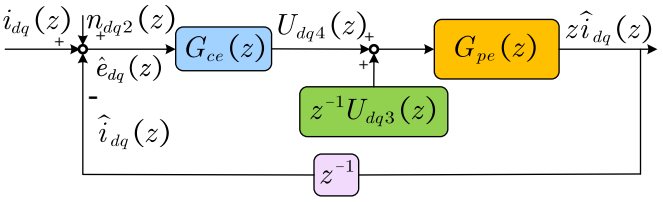

Fig. 5. The block diagram of the proposed current predictor.

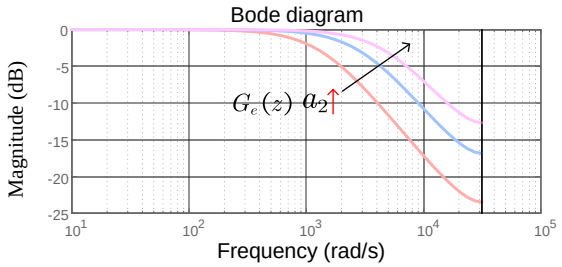

Fig. 6. Bode diagrams of the local noise suppression.

After obtaining the plant of the PMSM of the current predictor, the controller can be designed based on the IMC principle as follows:

$$\begin{aligned} G_{ce}(z) =& \frac{za_2}{z-1} G_{pe}^{-1}(z) \\ =& \frac{a_2\left(z-1+j\omega_e T_s+\left(R_s+R_a\right)L_s^{-1}T_s\right)}{L_s^{-1}T_s}, \end{aligned} \tag{28}$$

where a_2 is the bandwidth of the proposed current predictor which will be discussed in detail later. The block diagrams of the proposed current predictor is shown in Fig. 5.

Generally, the disturbance caused by parameter mismatches U_{dq4} need to be obtained and compensated to (4) and (5) in the ESO structure. However, since the input $i_{dq}(z)$, disturbance $z^{-1}U_{dq3}(z)$ and feedback coefficient z^{-1} have been already known, superior to ESO structures, there is no need to obtain complex U_{dq4} in the proposed structure, the output $z\hat{i}_{dq}(z)$ of the current predictor can be obtained based on the superposition theorem, i.e., the sum of the input signal effect and the disturbance signal effect:

$$\begin{aligned} z\hat{i}_{dq}(z) &= i_{dq}(z)\frac{G_{ce}(z)G_{pe}(z)}{1+z^{-1}G_{ce}(z)G_{pe}(z)} \\ &+ \frac{G_{pe}(z)}{1+z^{-1}G_{ce}(z)G_{pe}(z)} z^{-1}U_{dq3}(z) \\ &= i_{dq}(z)\frac{za_2}{z-1+a_2} \\ &+ \frac{z-1}{z-1+a_2}\frac{L_s^{-1}T_s z^{-1}U_{dq3}(z)}{1-z^{-1}+j\omega_e T_s z^{-1}+z^{-1}\left(R_s+R_a\right)T_s}. \end{aligned} \tag{29}$$

After designing the proposed predictor, the digital implementation can be derived as follows:

$$\begin{cases} M_{dq1}(k) = T_s U_{dq3}(k-1)L_s^{-1} \\ M_{dq2}(k) = M_{dq1}(k) \\ \qquad +M_{dq2}(k-1)\left(1-j\omega_e T_s-\left(R_s+R_a\right)L_s^{-1}T_s\right) \\ M_{dq3}(k) = M_{dq2}(k)-M_{dq2}(k-1)-(a_2-1)M_3(k-1) \\ M_{dq4}(k) = i_{dq}(k)a_2 - M_{dq4}(k-1)(a_2-1) \\ \hat{i}_{dq}(k+1) = M_{dq3}(k)+M_{dq4}(k). \end{cases} \tag{30}$$

By replacing $\hat{i}_{dq}(k+1)$ in (5) with $\hat{i}_{dq}(k+1)$ in the proposed current predictor, the proposed MPC can be implemented.

C. Local Analysis and Adaptive Control for the Proposed Predictor

1) Parameter sensitivity analysis: In order to analyze the parameter robustness of the current predictor, the transfer function of steady-state error $e_{dq2}(z)$ is derived as follows:

$$\begin{aligned} \lim_{t\to\infty}\hat{e}_{dq}(t) =& \lim_{z\to 1}(z-1)\hat{e}_{dq}(z) \\ =& \lim_{z\to 1}\Big(i_{dq}(z)\frac{G_{ce}(z)G_{pe}(z)}{1+z^{-1}G_{ce}(z)G_{pe}(z)} \\ &+ \frac{-(z-1)G_{pe}(z)}{1+z^{-1}G_{ce}(z)G_{pe}(z)} z^{-1}U_{dq3}(z)\Big) = 0. \end{aligned} \tag{31}$$

It can be seen from (31) that the steady error is equal to 0 when the parameter mismatch occurs, which means $\hat{i}_{dq}(t) = i_{dq}(t)$ and the proposed predictor has the good robustness.

2) Measurement noise suppression analysis: Since the feedback current is obtained through the proposed current predictor, it is necessary to analysis the noise suppression. Therefore, the transfer function from measurement noise n_{dq2} to the output $G_e(z)$ can be derived as follows:

$$G_e(z) = \frac{z\hat{i}_{dq}(z)}{n_{dq2}} = \frac{G_{ce}(z)G_{pe}(z)}{1+z^{-1}G_{ce}(z)G_{pe}(z)}. \tag{32}$$

Fig. 6 plots the frequency characteristics of $G_e(z)$. It can be seen from Fig. 6 that the noise suppression ability is decreased as a_2 increased. Meanwhile, a_2 can determine the dynamic performance of the proposed current predictor. Hence, the adjustment of a_2 is particularly critical for the MPC system. In this case, an novel adaptive control method based on the PI controller is proposed to adjust the coefficient of the current predictor between steady-state and dynamic conditions.

3) Adaptive controller: The proposed adaptive control is divided into four components: error calculation, dynamic and steady-state assessment, PI controller, and the stability guarantee. The error calculation $e_{dq2}(k)$ can be designed as follows:

$$\begin{aligned} e_{dq1}(k) =& i_{dq}^{ref}(k+2) - i_{dq}(k) \\ e_{dq2}(k) =& e_{dq1}(k)\,sgn\left(e_{dq1}\right), \end{aligned} \tag{33}$$

where sgn represents sign function and can be presented as follows:

$$sgn(x) = \begin{cases} 1\ if\ \ (x>0) \\ 0\ if\ \ (x=0) \\ -1\ if\ \ (x<0). \end{cases} \tag{34}$$

$e_{dq3}(k)$ is the input of the PI controller and can be acquired as follows:

$$e_{dq3}(k) = e_{dq2}(k) - e_{dq2\max}, \tag{35}$$

where $e_{dq2\max}$ is the part of dynamic and steady-state assessment and is set to 1.5A in this paper. When $e_{dq2}(k)$ greater

than $e_{dq2\max}$, the system is determined to be dynamic state, and a_2 will be gradually increased. When $e_{dq2}(k)$ smaller than $e_{dq2\max}$, the system is determined to be steady-state, and a_2 will be gradually decreased through the PI controller. It should be noted that $e_{dq2\max}$ can be configured according to different requirements and application conditions. Motivated by the approach proposed in [44], the adjustment of the two parameters of the PI controller has been simplified such that only a single bandwidth parameter α needs to be tuned, the proportional gain is set to αL_s, and the integral gain is set to αR_s. In this way, the PI controller can be presented as follows:

$$e_{dq3}\left(\alpha L_s + \alpha R_s \cdot T_s \cdot \frac{z}{z-1}\right) = a_2 \tag{36}$$

Furthermore, for the stability guarantee, according to the stability principle (poles are located inside the unit circle), the value of a_2 should be observed as $[0, 1]$. A more detailed explanation of the tuning of a_2 is as follows: as the bandwidth adjustment parameter of the current predictor, the value of a_2 has a significant impact on both the dynamic response and noise immunity of the system. When a_2 is set to a relatively large value, the current predictor can respond more rapidly to changes in current, which is beneficial for improving the system's dynamic performance and its ability to quickly compensate for disturbances. However, a larger bandwidth also amplifies high-frequency measurement noise within the system, which may increase the noise component in the feedback current signal of the system and adversely affect the steady-state performance. Therefore, during steady-state operation, the value of a_2 can be appropriately reduced to effectively suppress high-frequency noise and improve the steady-state accuracy of the system. Conversely, when the system is subject to disturbances or requires a rapid dynamic response, the value of a_2 can be increased to enhance the dynamic response capability. By adaptively adjusting a_2 according to the operating state of the system, a balance between steady-state and dynamic performance can be achieved, enabling smoother transitions between these two modes. The block diagram of the proposed adaptive controller is shown in Fig. 3.

D. Implementation of Triple-vector MPC

As the reference dq current has been converted into the reference voltage with the active damping term incorporated, a triple vector MPC approach is employed to achieve the reference voltage tracking in this part. Its main difference between the existing SVPWM approach and the multiple vector MPC lies in the way to calculate the dwell time of different voltage vectors [14]. The SVPWM approach is based on the voltage-second balance law while the MPC approach is mainly based on the numerical value of cost function. Specifically, the three different voltage vector that produces smallest cost function value will be applied for the next control cycle.

$$J_2 = \left\| u^*_{dq}(k+1) - u_{dq}(k+1) \right\|_2 \tag{37}$$

For a simple implementation, the dwell time for each vector can be calculated with the value of their corresponding cost function values [18]. The relationship among the three voltage vectors is devised as

$$\begin{cases} \frac{t_1}{T_s} + \frac{t_2}{T_s} + \frac{t_3}{T_s} = 1 \\ u^*_{dq} = \frac{t_1}{T_s} u_1 + \frac{t_2}{T_s} u_2 + \frac{t_3}{T_s} u_3 \\ 0 \le t_1, t_2, t_3 \le T_s \end{cases} \tag{38}$$

Here, the duration time for a voltage vector is inversely proportional to its cost function value. Hence, the derivation can be given as:

$$\begin{cases} d_1 = \frac{J_2^{opt2} J_2^{opt3}}{J_2^{opt1} J_2^{opt2} + J_2^{opt2} J_2^{opt3} + J_2^{opt1} J_2^{opt3}} \\ d_2 = \frac{J_2^{opt1} J_2^{opt3}}{J_2^{opt1} J_2^{opt2} + J_2^{opt2} J_2^{opt3} + J_2^{opt1} J_2^{opt3}} \\ d_3 = \frac{J_2^{opt1} J_2^{opt2}}{J_2^{opt1} J_2^{opt2} + J_2^{opt2} J_2^{opt3} + J_2^{opt1} J_2^{opt3}} \end{cases} \tag{39}$$

Where d_1, d_2, and d_3 are the duty cycle of the three selected voltage vectors, respectively.

For the triple vector MPC in three level inverter drive, the small voltage vector will be always selected to synthesize the switching sequence. Hence, the neutral point voltage is balanced by adjust the dwell time of the small voltage vector pairs. If d_1 is the duty cycle of the small voltage vector pairs, it should be assigned to the P-type small vector and the N-type small vector, and the duty cycle is adjusted to balance the neutral point voltage. A proportional gain factor with respect to the neutral point voltage can be thereby defined as

$$\begin{cases} g_{np} = \frac{\lambda(V_{c2} - V_{c1})}{(V_{c2} + V_{c1})} \\ -1 \le g_{np} \le 1 \end{cases} \tag{40}$$

Then, the duty cycle for P vector can be $0.5d_1(1 - g_{np})$, while for N vector is $0.5d_1(1 + g_{np})$. For example, the duty cycle of the positive small voltage vectors will increase once the upper dc-link capacitor voltage V_{c2} is greater than the lower dc-link capacitor voltage V_{c1}.

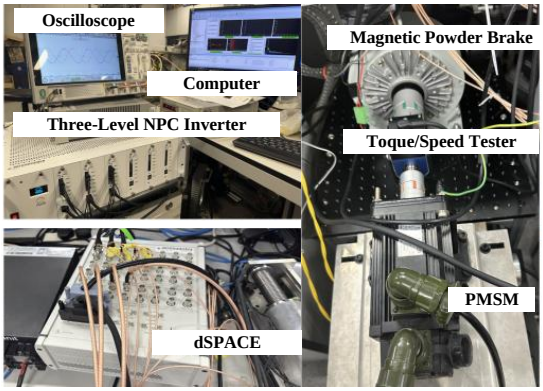

Fig. 7. Test rig of the PMSM platform.

IV. EXPERIMENT RESULTS

A. Experimental Setup

In this section, to better validate the properties of the proposed method, experiments of the conventional TVMPC , ultra-local model MPC with ESO (ULM-ESO) [45], and the proposed method in one PMSM system were carried out. The

TABLE I
PARAMETERS OF THE PMSM PLATFORM.

Parameters	Value	Unit
Pole pair (p)	4	
Rated power (P_n)	1.5	kW
d-axis inductance (L_d)	1.95	mH
q-axis inductance (L_q)	1.95	mH
Stator resistance (R_s)	0.65	Ω
Rotor flux linkage (ψ_f)	0.135	Wb
Sampling time (T_s)	100	μs

PMSM test platform is shown in Fig. 7. The oscilloscope is the high performance Rigol DHO1204. The three-level NPC inverter and the MicroLabBox dSPACE 1202 are adopted to execute control algorithms. The load torque is provided with the help of a magnetic powder brake. The parameters of the PMSM and the controller are listed in Table I.

B. Steady-state Performance Evaluation

Since the steady-state performance can be used to evaluate the controller's noise suppression and tracking ability, the steady-state performance of the three controllers is first tested at different rotor speeds. In order to make a fair comparison, the bandwidths of the UML-ESO are set to 100 Hz and 400 Hz, respectively. In addition, the total harmonic distortion (THD) is used to measure steady-state performance and the load torque is set to 5 Nm. It can be seen from Fig. 8 and Table II that under the condition of 100 RPM, the THD of the TVMPC is 2.76%, ULM-ESO with $\omega_n = 100$Hz is 4.67%, and ULM-ESO with $\omega_n = 400$Hz is 4.43%. Increasing the bandwidth of the ESO can effectively suppress external disturbances and achieve better current tracking performance, but it also amplifies high-frequency noise [35]. However, the proposed controller significantly reduces the THD to only 2.47%. When the rotor speed is increased to 1000 RPM, it can be seen from Fig. 8 (f), (g) and (h) that the THD of the TVMPC changes to 4.24%, ULM-ESO with $\omega_n = 100$Hz is 7.12%, and ULM-ESO with $\omega_n = 400$Hz is 6.83%., while the THD of the proposed controller still remains significantly lower than that of the ULM-ESO, at only 4.72%.

Furthermore, in order to verify the validity of the proposed current predictor on measurement noise suppression and the proposed adaptive control method, different value of a_2 are forced to evaluate the steady-state performance. It can be seen that under 100 RPM rotor condition, the THD increases as the value of a_2 increases. When $a_2 = 0.3$, the THD is 2.50%, and it rises to 3.32% when $a_2 = 0.6$. Similar results are observed at 1000 RPM, where the THD is 4.87% when $a_2 = 0.3$ and increases to 5.07% when $a_2 = 0.6$. Frequency-domain noise suppression analysis for different value of a_2 are shown in Fig. 9. It can be observed that as a_2 increases, the proportion of high-frequency components gradually increases. Therefore, the proposed adaptive control method and the coefficient a_2 can enhance the system's noise suppression and smooth the current.

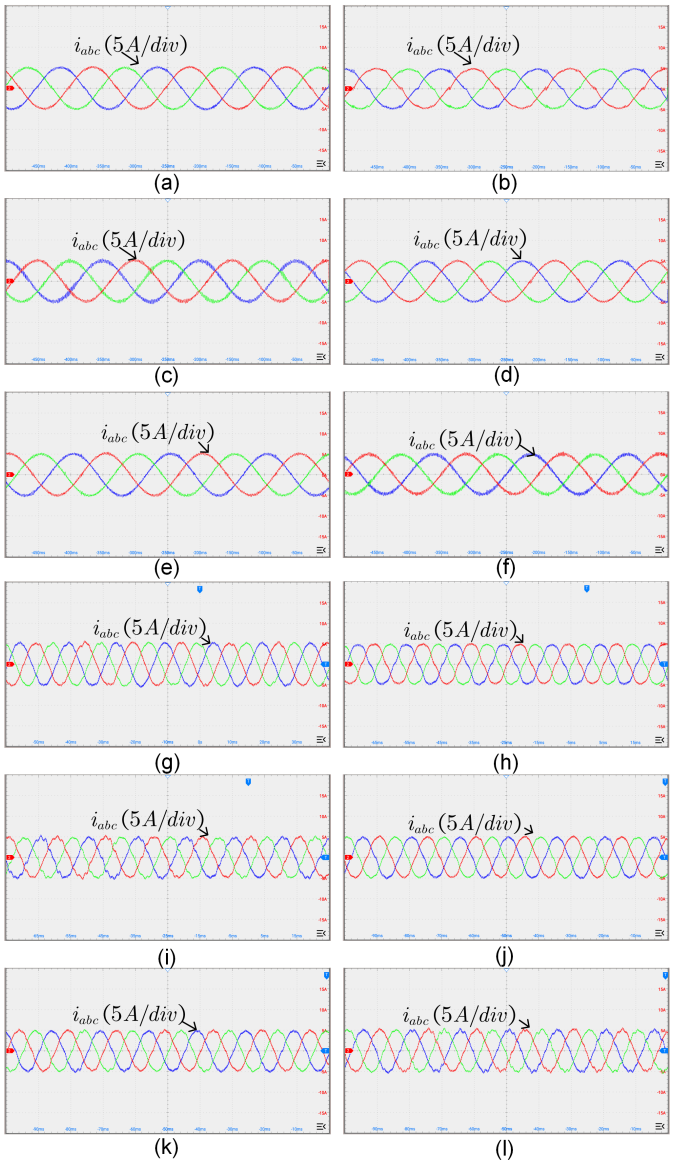

Fig. 8. Steady state performance evaluation in different rotor speed conditions. (a) TVMPC with 100 rpm rotor speed. (b) ULM-ESOC with 100 rpm rotor speed and $\omega_n = 100$Hz. (c) ULM-ESOC with 100 rpm rotor speed and $\omega_n = 400$Hz. (d) Proposed method with 100 rpm rotor speed. (e) Proposed method with 100 rpm rotor speed and $a_2 = 0.3$. (f) Proposed method with 100 rpm rotor speed and $a_2 = 0.6$. (g) TVMPC with 1000 rpm rotor speed. (h) ULM-ESOC with 1000 rpm rotor speed and $\omega_n = 100$Hz. (i) ULM-ESOC with 1000 rpm rotor speed and $\omega_n = 400$Hz (j) Proposed method with 1000 rpm rotor speed. (k) Proposed method with 1000 rpm rotor speed and $a_2 = 0.3$. (l) Proposed method with 100 rpm rotor speed and $a_2 = 0.6$.

C. Neutral Point Voltage Balance Evaluation

The DC-capacitor voltage of different methods under reference speed step scenario is provided in Fig. 10. It can be seen that the neutral point voltage can be well balanced in all operation conditions and thereby the effectiveness of the proposed method is verified.

D. Dynamic Response Performance Evaluation

Conventional MPC has been widely noticed and used because of its fast dynamic response. Hence, the experiments of

TABLE II
STEADY-STATE COMPARISON OF CONTROLLERS UNDER DIFFERENT SPEED.

Controller	Speed (rpm)	THD (%)
TV-MPC	100	2.76
ULM-ESO with $\omega_n = 100$Hz	100	4.67
ULM-ESO with $\omega_n = 400$Hz	100	4.43
Proposed controller	100	2.47
Proposed controller with $a_2 = 0.3$	100	2.50
Proposed controller with $a_2 = 0.6$	100	3.32
TV-MPC	1000	4.24
ULM-ESO with $\omega_n = 100$Hz	1000	7.12
ULM-ESO with $\omega_n = 400$Hz	1000	6.83
Proposed controller	1000	4.72
Proposed controller with $a_2 = 0.3$	1000	4.87
Proposed controller with $a_2 = 0.6$	1000	5.07

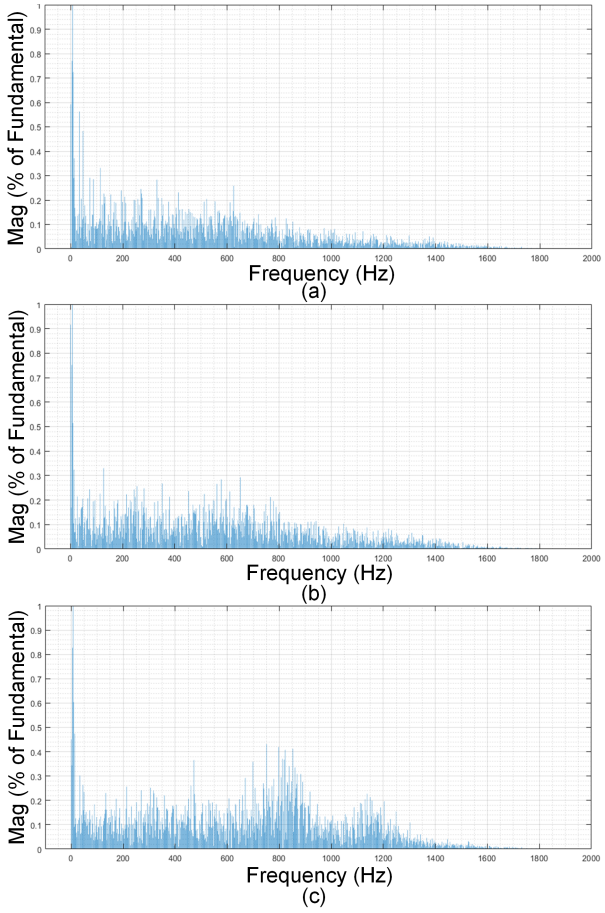

Fig. 9. Frequency-domain noise suppression analysis for different value of a_2. (a) adaptive control. (b) $a_2 = 0.3$. (c) $a_2 = 0.6$.

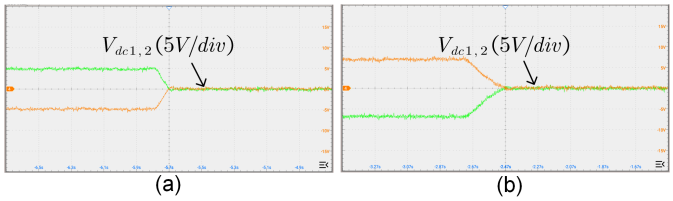

Fig. 10. DC-link capacitor voltage of the proposed method under steady state. (a) 100 rpm. (b) 1000 rpm.

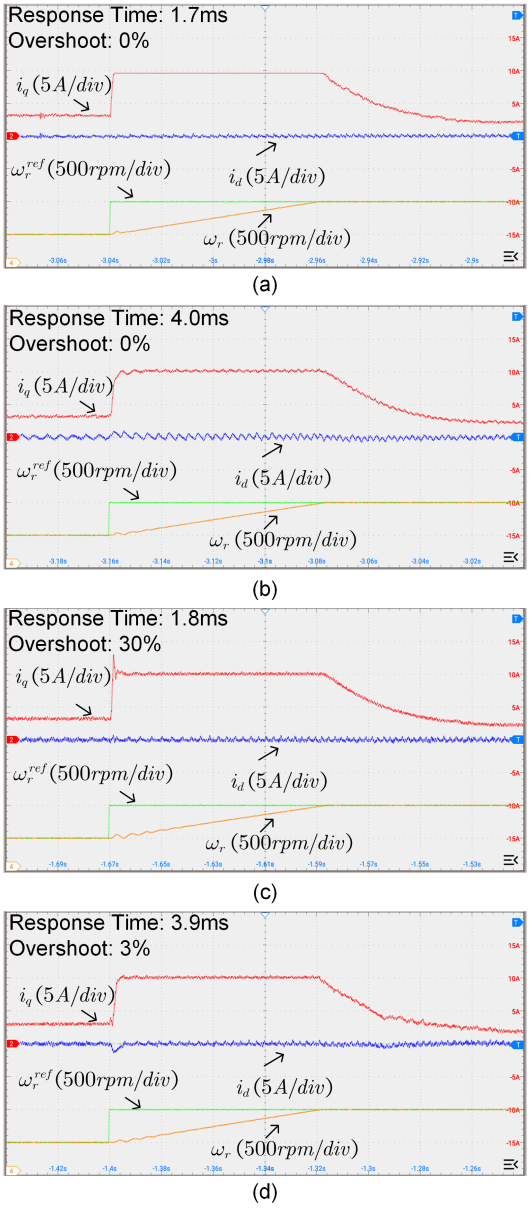

Fig. 11. Dynamic response performance evaluation (500 rpm to 1000 rpm). (a) TVMPC. (b) ULM-ESO with $\omega_n = 100$Hz. (c) ULM-ESO with $\omega_n = 400$Hz. (d) Proposed controller.

dynamic response are carried out in this section. The reference rotor speed is creased from 500 rpm to 1000 rpm, and the load torque is kept constant during the transient. The dq-axis current and speed waveform are shown in Fig. 11. It can be seen that the TVMPC has the shortest response time (1.7 ms) and has no overshoot compared to other controllers. ULM-ESO with $\omega_n = 100$Hz has the longest response time. Although increasing the bandwidth of the ESO can improve the response perofmrance, it also introduce a certain degree of overshoot (30%). The proposed controller achieves a short response time

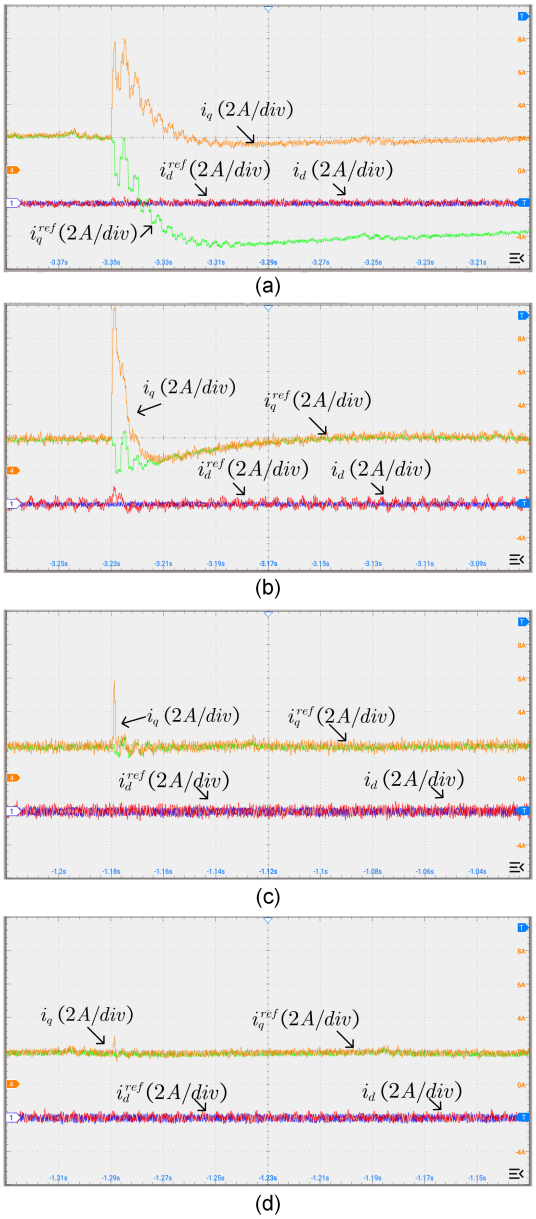

Fig. 12. Disturbance rejection performance evaluation. (a) TVMPC. (b) ULM-ESO with $\omega_n = 100$Hz. (c) ULM-ESO with $\omega_n = 400$Hz. (d) Proposed method.

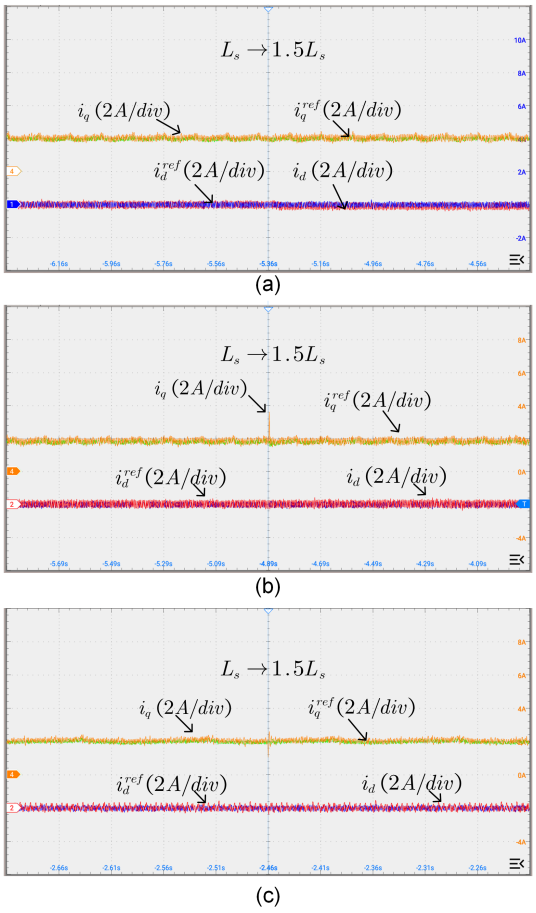

Fig. 13. Parameter robustness performance evaluation. (a) TVMPC with the inductance mismatch. (b) ULM-ESO with the inductance mismatch. (c) Proposed controller with the inductance mismatch.

(3.9 ms) while maintaining a low overshoot (3%). Hence, the fast dead-beat response using the conventional dead-beat voltage prediction can be also achieved by the proposed controller. In addition, the proposed controller exhibits smoother current compared to other methods, which indicates a stronger noise suppression ability.

E. Disturbance Rejection Performance Evaluation

Disturbance rejection ability is a key factor in control systems, which is why the ESO and active damping have been widely used. Hence, the experiment of disturbance rejection is carried out in this section to validate the disturbance rejection and the ability to balance the coupling between the noise suppression and disturbance rejection. The external disturbance is generated by a sudden back electromotive voltage change in the feedforward path of the current loop. In order to make a fair comparison, the bandwidths of the UML-ESO are set to 100 Hz and 400 Hz, respectively. It can be seen from Fig. 12 that the TVMPC exhibits pronounced current oscillations, along with a noticeable current offset. In ULM-ESO, as the bandwidth increases, the system's disturbance rejection capability is enhanced, and both the amplitude and duration of current oscillations are significantly reduced. However, since a higher bandwidth amplifies high-frequency noise, a noticeable decrease in current smoothness can be observed. Compared to other controllers, the proposed controller exhibits the best disturbance rejection capability and the smallest current oscillations, while also achieving the highest current smoothness. Therefore, it can fully illustrate that the proposed controller can decouple the coupling issue between disturbance rejection and noise suppression effectively.

F. Parameter Robustness Performance Evaluation

In practical operating conditions, the inductance parameters vary with changes in current due to magnetic saturation. Therefore, it is necessary to conduct parameter robustness experiments. It should be noted that the parameters in the controller are adjusted to simulate the parameter mismatch

TABLE III
EXECUTION TIME OF DIFFERENT MPC METHODS.

Controller	Turnaround time
SV-MPC	21.2 μs
TVMPC	23.7 μs
ULM-ESO	23.8 μs
Proposed Method	24.0 μs

condition. In the case of reduced inductance, i.e., suddenly setting the inductance parameter in the controller to 1.5 times the motor's initial inductance, it can be seen from Fig. 13 (a) that after parameter mismatch occurs, the d-axis current of TVMPC exhibits a slight offset, and the current smoothness deteriorates. Current oscillations occurred with both the ULM-ESO and the proposed controller, but the system rapidly returned to steady state in each case. It is noteworthy that the magnitude of oscillations with the proposed controller was significantly lower than that observed with the ULM-ESO. Hence, the proposed controller can achieve better parameter robustness performance compared to the TVMPC and ULM-ESO.

G. Execution Time Evaluation

The execution times of four MPC methods on the dSPACE controller were evaluated, as summarized in TABLE III. The turnaround time for the single vector MPC (SV-MPC) method is 21.2 μs, whereas the TVMPC methods exhibit an increase of approximately 2.5 μs due to the additional computation required for more voltage vectors . Notably, the proposed method introduces only a slight increase in computational cost, which is negligible when compared to the TVMPC and ULM-ESO. Therefore, it can be fully validated that the proposed method has low computational burden and can be utilized in practice.

V. CONCLUSION

This study presents a novel robust MPC strategy for electrical drive systems, aiming at the enhancements in both disturbance rejection and noise suppression. The proposed controller consists of three key components: First, an active resistance feedback term was incorporated into the triple-vector MPC framework as an alternative to the conventional extended state observer, resulting in better disturbance rejection capabilities. Second, a novel discrete-time current predictor was developed to achieve an independent current estimation, with analytical results confirming that noise suppression can be effectively optimized through precise adjustment of the current predictor coefficient. Third, an adaptive parameter adjustment mechanism based on tracking error was implemented to ensure both rapid tracking response and excellent steady-state performance.

Comprehensive comparative evaluations were conducted on a PMSM drive test bench, comparing the proposed controller with conventional ESO-based MPC. The experimental results revealed that: (1) In steady-state performance evaluation, the proposed controller demonstrated superior total harmonic distortion (THD) characteristics compared to ULM-ESO, effectively addressing the coupling issue between disturbance rejection and noise suppression; (2) Dynamic response evaluation showed that the proposed controller maintains comparable dynamic performance to tvMPC and ULM-ESO while preserving the fast dead-beat response characteristic; (3) Disturbance rejection tests indicated that the proposed controller exhibits smaller average oscillation amplitudes than TVMPC and ULM-ESO; (4) Parameter robustness analysis confirmed the controller's insensitivity to inductance variations, maintaining stable performance under parameter deviations. The proposed controller exhibits three distinctive advantages: enhanced noise suppression capability, rapid dynamic response characteristics, and robust parameter insensitivity. These features make it particularly suitable for electric vehicle applications where high-performance motor control is essential.

REFERENCES

[1] L. Dai, S. Niu, J. Gao, K. Liu, S. Huang, and W. L. Chan, "Diverse slot-opening designs for cogging torque and performance optimization in PM machines," *IEEE Trans. Transport. Electrific.*, DOI 10.1109/TTE.2025.3540837, pp. 1–1, 2025.

[2] H. Zhan, W. Liu, Z. Lyu, S. Niu, L. Wu, and K. T. Chau, "Eccentricity fault diagnosis in multimodule permanent magnet synchronous machines based on zero-sequence voltage component," *IEEE Trans. Ind. Electron.*, DOI 10.1109/TIE.2025.3574542, pp. 1–11, 2025.

[3] Y. Zhang, W. Shen, H. Yang, X. Guo, M. Fu, and M. Qin, "An improved model-free predictive current control method for PMSM drives based on extended control set and fast current difference updating," in *2022 IEEE Energy Conversion Congress and Exposition (ECCE)*, pp. 1–8, 2022.

[4] Z. Lyu, S. Niu, M. Hu, T. Wang, L. Wu, K. T. Chau, and W. L. Chan, "Improving DC-Link voltage utilization in PMSM drives with resistance asymmetry via active harmonic injection," *IEEE Trans. Transport. Electrific.*, DOI 10.1109/TTE.2024.3524634, pp. 1–1, 2024.

[5] X. Yuan, J. Wen, S. Niu, and M. Hu, "High damped digital current controller based on active resistance for ac machines," *IEEE Trans. Ind. Electron.*, DOI 10.1109/TIE.2025.3567673, pp. 1–11, 2025.

[6] X. Zhang, B. Hou, and Y. Mei, "Deadbeat predictive current control of permanent-magnet synchronous motors with stator current and disturbance observer," *IEEE Trans. Power Electron.*, vol. 32, no. 5, pp. 3818–3834, May 2017.

[7] Y. Zhang, D. Xu, J. Liu, S. Gao, and W. Xu, "Performance improvement of model-predictive current control of permanent magnet synchronous motor drives," *IEEE Trans. Ind. Appl.*, vol. 53, no. 4, pp. 3683–3695, Aug. 2017.

[8] S. Vazquez, J. Rodriguez, M. Rivera, L. G. Franquelo, and M. Norambuena, "Model predictive control for power converters and drives: advances and trends," *IEEE Trans. Ind. Electron.*, vol. 64, no. 2, pp. 935–947, Feb. 2017.

[9] X. Tang, S. Niu, K. T. Chau, X. Yuan, and W. L. Chan, "Model predictive control of three-level NPC inverter-fed PMSM drives based on a novel vector-selection scheme." *IEEE J. Emerg. Sel. Top. Power Electron., Early Access*.

[10] X. Tang and S. Niu, "Coherent vector based model predictive control with zero-sequence component injection for three-level npc inverter fed pmsm drives," *IEEE Trans. Power Electron.*, DOI 10.1109/TPEL.2025.3578425, pp. 1–11, 2025.

[11] F. Wang, S. Li, X. Mei, W. Xie, J. RodrÃguez, and R. M. Kennel, "Model-based predictive direct control strategies for electrical drives: An experimental evaluation of ptc and pcc methods," *IEEE Trans. Ind. Infor.*, vol. 11, DOI 10.1109/TII.2015.2423154, no. 3, pp. 671–681, 2015.

[12] Z. Sun, J. Wen, X. Yuan, G. Ma, S. Niu, and K. Chau, "A novel robust dead-beat structure for double vector model predictive control in three-level inverter fed pmsm drives," *IEEE Trans. Power Electron.*, DOI 10.1109/TPEL.2025.3575075, pp. 1–11, 2025.

[13] Y. Zhang and H. Yang, "Model predictive torque control of induction motor drives with optimal duty cycle control," *IEEE Trans. Power Electron.*, vol. 29, no. 12, pp. 6593–6603, Dec. 2014.

[14] Y. Yang, H. Wen, R. Chen, M. Fan, X. Zhang, M. Norambuena, and J. Rodriguez, "An efficient model predictive control using virtual voltage vectors for three-phase three-level converters with constant switching frequency," *IEEE Trans. Ind. Electron.*, vol. 69, DOI 10.1109/TIE.2021.3075890, no. 4, pp. 3998–4009, 2022.

[15] D. Liu, W. Xu, H. Xiao, P. Zhong, and L. Guo, "An improved triple-vector modulated model predictive control method for permanent magnet synchronous motor," in *2023 IEEE International Conference on Predictive Control of Electrical Drives and Power Electronics (PRECEDE)*, DOI 10.1109/PRECEDE57319.2023.10174331, pp. 1–5, 2023.

[16] Z. Zhang, H. Fang, F. Gao, J. RodrÃguez, and R. Kennel, "Multiple-vector model predictive power control for grid-tied wind turbine system with enhanced steady-state control performance," *IEEE Trans. Ind. Electron.*, vol. 64, DOI 10.1109/TIE.2017.2682000, no. 8, pp. 6287–6298, 2017.

[17] X. Wang and D. Sun, "Three-vector-based low-complexity model predictive direct power control strategy for doubly fed induction generators," *IEEE Trans. Power Electron.*, vol. 32, DOI 10.1109/TPEL.2016.2532387, no. 1, pp. 773–782, 2017.

[18] L. Guo, M. Chen, Y. Li, P. Wang, N. Jin, and J. Wu, "Hybrid multi-vector modulated model predictive control strategy for voltage source inverters based on a new visualization analysis method," *IEEE Trans. Transport. Electrific.*, vol. 9, DOI 10.1109/TTE.2022.3161583, no. 1, pp. 8–21, 2023.

[19] S. W. Kang, J. H. Soh, and R. Y. Kim, "Symmetrical three-vector-based model predictive control with deadbeat solution for ipmsm in rotating reference frame," *IEEE Trans. Ind. Electron.*, vol. 67, DOI 10.1109/TIE.2018.2890490, no. 1, pp. 159–168, 2020.

[20] X. Yuan, S. Zhang, C. Zhang, A. Galassini, G. Buticchi, and M. Degano, "Improved model predictive current control for SPMSM drives using current update mechanism," *IEEE Trans. Ind. Electron.*, vol. 68, no. 3, pp. 1938–1948, Mar. 2021.

[21] Y. Wei, H. Young, D. Ke, F. Wang, H. Qi, and J. RodrÃguez, "Model-free predictive control using sinusoidal generalized universal model for PMSM drives," *IEEE Trans. Ind. Electron.*, vol. 71, no. 11, pp. 13 720–13 731, Nov. 2024.

[22] S. Zhu, W. Huang, Y. Yan, and Z. Niu, "High-damped complex vector current regulator for PMSM based on active damping function," *IEEE Trans. Power Electron.*, vol. 38, no. 4, pp. 5204–5216, Apr. 2023.

[23] D. Ke, F. Wang, X. Yu, S. A. Davari, and R. Kennel, "Predictive error model-based enhanced observer for PMSM deadbeat control systems," *IEEE Trans. Ind. Electron.*, vol. 71, no. 3, pp. 2242–2252, Mar. 2024.

[24] Z. Lyu, S. Niu, H. Zhan, T. Wang, L. Wu, and K. T. Chau, "Harmonic current suppression for pmsm drives via time-shifting harmonic extraction," *IEEE Trans. Ind. Electron.*, DOI 10.1109/TIE.2025.3572978, pp. 1–11, 2025.

[25] S. Yang, Z. Yin, C. Tong, Y. Sui, and P. Zheng, "Active damping current control for current-source inverter-based pmsm drives," *IEEE Trans. Ind. Electron.*, vol. 70, DOI 10.1109/TIE.2022.3176270, no. 4, pp. 3549–3560, 2023.

[26] J. Wen, X. Yuan, S. Niu, and W. L. Chan, "A robust complex vector pi current controller with deadbeat response for PMSM drives," *IEEE Trans. Ind. Electron., Early Access*, 2024.

[27] F. Briz, M. Degner, and R. Lorenz, "Analysis and design of current regulators using complex vectors," *IEEE Trans. Ind. Appl.*, vol. 36, no. 3, pp. 817–825, May 2000.

[28] S. Zhu, W. Huang, Y. Yan, and Z. Niu, "High-damped complex vector current regulator for pmsm based on active damping function," *IEEE Trans. Power Electron.*, vol. 38, DOI 10.1109/TPEL.2022.3230350, no. 4, pp. 5204–5216, 2023.

[29] S. N. Vukosavic, L. S. Peric, and E. Levi, "Digital current controller with error-free feedback acquisition and active resistance," *IEEE Trans. Ind. Electron.*, vol. 65, DOI 10.1109/TIE.2017.2745476, no. 3, pp. 1980–1990, 2018.

[30] A. G. Yepes, A. Vidal, J. Malvar, O. Lopez, and J. Doval-Gandoy, "Tuning method aimed at optimized settling time and overshoot for synchronous proportional-integral current control in electric machines," *IEEE Trans. Power Electron.*, vol. 29, DOI 10.1109/TPEL.2013.2276059, no. 6, pp. 3041–3054, 2014.

[31] O. Babayomi and Z. Zhang, "Model-free predictive control of power converters with multifrequency extended state observers," *IEEE Trans. Ind. Electron.*, vol. 70, no. 11, pp. 11 379–11 389, Nov. 2023.

[32] A. A. Godbole, J. P. Kolhe, and S. E. Talole, "Performance analysis of generalized extended state observer in tackling sinusoidal disturbances," *IEEE Control Syst*, vol. 21, no. 6, pp. 2212–2223, Nov. 2013.

[33] X. Yang, H. Hu, H. Hu, Y. Liu, and Z. He, "A quasi-resonant extended state observer-based predictive current control strategy for three-phase PWM rectifier," *IEEE Trans. Ind. Electron.*, vol. 69, no. 12, pp. 13 910–13 917, Dec. 2022.

[34] R. Madonski and P. Herman, "Method of sensor noise attenuation in high-gain observers experimental verification on two laboratory systems," in *2012 IEEE International Symposium on Robotic and Sensors Environments Proceedings*, pp. 121–126, 2012.

[35] S. Zhu, W. Huang, Y. Zhao, X. Lin, D. Dong, W. Jiang, Y. Zhao, and X. Wu, "Robust speed control of electrical drives with reduced ripple using adaptive switching high-order extended state observer," *IEEE Trans. Power Electron.*, vol. 37, no. 2, pp. 2009–2020, Feb. 2022.

[36] K. Lakomy, R. Madonski, B. Dai, J. Yang, P. Kicki, M. Ansari, and S. Li, "Active disturbance rejection control design with suppression of sensor noise effects in application to dc-dc buck power converter," *IEEE Trans. Ind. Electron.*, vol. 69, no. 1, pp. 816–824, Jan. 2022.

[37] S. Ahmad and A. Ali, "On active disturbance rejection control in presence of measurement noise," *IEEE Trans. Ind. Electron.*, vol. 69, no. 11, pp. 11 600–11 610, Nov. 2022.

[38] X. Yuan, Y. Zuo, Y. Fan, and C. H. T. Lee, "Model-free predictive current control of SPMSM drives using extended state observer," *IEEE Trans. Ind. Electron.*, vol. 69, no. 7, pp. 6540–6550, Jul. 2022.

[39] H. Cao, Y. Deng, Y. Zuo, X. Liu, J. Wang, and C. H. T. Lee, "A variable structure adrc for enhanced disturbance rejection and improved noise suppression of pmsm speed system," *IEEE Trans. Ind. Electron.*, vol. 72, DOI 10.1109/TIE.2024.3468613, no. 5, pp. 4481–4495, 2025.

[40] M. Yang, S. Huang, W. Liao, X. Wu, J. Kang, G. Liang, T. Wu, and S. Huang, "Nonparametric predictive current control for SPMSM with adaptive cascade extended noise state observer," *IEEE Trans. Power Electron.*, vol. 40, no. 1, pp. 1717–1727, Jan. 2025.

[41] X. Feng, S. Xie, P. Gu, Z. Lei, W. Zhang, and C. Zhao, "Measurement noise suppression of ipmsm speed loop based on fuzzy linear extend state observer," in *2023 International Conference on Power Energy Systems and Applications (ICoPESA)*, DOI 10.1109/ICoPESA56898.2023.10141432, pp. 809–815, 2023.

[42] X. Yuan, S. Xie, J. Chen, S. Zhang, C. Zhang, and C. H. T. Lee, "An enhanced deadbeat predictive current control of SPMSM with linear disturbance observer," *IEEE J. Emerg. Sel. Top. Power Electron*, vol. 10, no. 5, pp. 6304–6316, Oct. 2022.

[43] M. Hu, W. Hua, Z. Wu, and Y. Hu, "Discrete-time current control of salient machines with a simplified model," *IEEE Trans. Ind. Electron.*, vol. 70, no. 7, pp. 6686–6698, Jul. 2023.

[44] L. Harnefors and H.-P. Nee, "Model-based current control of ac machines using the internal model control method," *IEEE Trans. Ind. Appl.*, vol. 34, DOI 10.1109/28.658735, no. 1, pp. 133–141, 1998.

[45] Z. Zhu, X. Wei, R. Han, C. Liu, and Z. Zhang, "Double-vector model-free predictive current control for pmsms with influence rejection of dc voltage mismatch," *IEEE Trans. Transport. Electrific.*, vol. 11, DOI 10.1109/TTE.2024.3498950, no. 2, pp. 6143–6153, 2025.

Junkai Wen received the B.Eng. degree in electrical engineering and automation from the Shanghai Ocean University, Shanghai, China, in 2021, and the M.Sc. degree in electrical power system with Distinction from University of Birmingham, Birmingham, U.K., in 2022. He is currently working toward the Ph,D. degree in electrical engineering with the Department of Electrical and Electronic Engineering, The Hong Kong Polytechnic University, Hong Kong, China.

His research interests include AC motor drives and power electronics.

Zhenyao Sun received the B.Sc. and M.Sc. degrees in Vehicle Engineering from Beijing Forestry University, Beijing, China, and Xihua University, Chengdu, China, in 2015 and 2019, respectively, and the Ph.D. degree in Vehicle Application Engineering from Southwest Jiaotong University, Chengdu, China, in 2024.

From 2022 to 2023, he was a Joint Ph.D. student at The University of British Columbia, Vancouver, BC, Canada. Since 2024, he has been a Postdoctoral Fellow at The Hong Kong Polytechnic University, Hong Kong. His research focuses on advanced control strategies for multilevel power converters and electric motor drives.

Xin Yuan (Senior Member, IEEE) received a Ph.D. in electrical engineering from the Beijing Institute of Technology, Beijing, China. He joined the Department of Electronic and Electrical Engineering at the University of Strathclyde in 2025, worked as a Senior Lecturer (Associate Professor). Before joining the University of Strathclyde, He worked as a Lecturer (Assistant Professor) at the School of Engineering of the University of Aberdeen, Research Assistant Professor at the Department of Electrical and Electronic Engineering of Hong Kong Polytechnic University, Hong Kong, and Research Associate at the PEMC Group of the University of Nottingham, UK. In 2020, he received a Ph.D. in electrical engineering from the Beijing Institute of Technology, Beijing, China, and he was also a Postdoctoral Research Fellow with the School of Electrical and Electronic Engineering, Nanyang Technological University, Singapore, from 2020 to 2022.

His speciality mainly contains the high-efficiency/fault-tolerant/low switching frequency/EMI suppression AC machine control and high-power density integrated multilevel WBG power converter hardware design with EMI suppression. Dr. Yuan has published over 50 academic papers and 4 patents, and served as a Guest Editor, Technical Track Chair, Special Session Chair, Associate Editor and Reviewer in different international journals and conferences.

Shuangxia Niu (Senior Member, IEEE) received the B.Sc. and M.Sc. degrees from Tianjin University, Tianjin, China, in 2002 and 2005, and the Ph.D. degree from the University of Hong Kong, Hong Kong, SAR, China, in 2009, all in electrical engineering.

She is currently a professor with the Department of Electrical and Electronic Engineering, The Hong Kong Polytechnic University. She authored or coauthored more than 200 papers in leading journals.

Prof. Niu is currently an Associate Editor for the IEEE Transactions on Industrial Electronics and the IEEE Journal of Emerging and Selected Topics in Power Electronics. She is Distinguish Lecturer of IEEE Vehicular Technology Society.

Zekai Lyu (Member, IEEE) received the B.Eng. degree from Southwest Jiaotong University, Chengdu, China, in 2018, the M.Sc. degree from Harbin Institute of Technology, Harbin, China, in 2020, and the Ph.D. degree from Zhejiang University, Hangzhou, China, in 2024, all in electrical engineering.

He is currently a Postdoctoral Fellow with the Department of Electrical and Electronic Engineering, The Hong Kong Polytechnic University, Hong Kong SAR, China. His research interests include control and condition monitoring of electric machine drive systems.

Kwok-tong Chau (Fellow, IEEE) received the B.Sc. (Eng.), M.Phil., and Ph.D. degrees in electrical and electronic engineering from The University of Hong Kong, Hong Kong, in 1988, 1991, and 1993, respectively. Currently, he serves as Chair Professor of Electrical Energy Engineering at the Research Centre for Electric Vehicles and Department of Electrical and Electronic Engineering, The Hong Kong Polytechnic University. His research interests include electric and hybrid vehicles, power electronics and drives, and renewable energies. He is the author of nine books and more than 350 journal papers.

Prof. Chau is a Fellow of the Institution of Engineering and Technology (IET), U.K., and of the Hong Kong Institution of Engineers. He is also a Coeditor of the Journal of Asian Electric Vehicles. He is a Chartered Engineer. He was the recipient of the Changjiang Chair Professorship from the Ministry of Education, China, and the Environmental Excellence in Transportation Award for Education, Training, and Public Awareness from the Society of Automotive Engineers International.